

Probing Circumstellar Material and Shock Acceleration in Core-Collapse Supernovae with High-Energy Neutrinos

Yi-Long Duan,¹ Tuohuniyazi Tuniyazi,¹ and Gang Guo^{1, 2, *}

¹*School of Mathematics and Physics, China University of Geosciences, Wuhan 430074, China*

²*Shenzhen Research Institute of China University of Geosciences, Shenzhen 518057, China*

We study high-energy (HE) neutrino production from interactions between supernova (SN) ejecta and the surrounding circumstellar material (CSM), focusing on regular Type II and Type IIn SNe. Using observationally inferred CSM density distributions, we calculate the resulting neutrino fluxes and examine their dependence on key parameters, including the CSM density normalization D_* , outer radius R_{csm} , proton acceleration efficiency ϵ_p , and magnetic energy fraction ϵ_B . Detection prospects are assessed with a binned likelihood analysis for IceCube, indicating that nearby SNe with moderately dense, confined CSM can produce detectable signals, with a typical detection horizon of $\sim 0.1\text{--}1$ Mpc. For a Galactic SN at ~ 10 kpc, high-statistics neutrino data with detailed temporal and spectral information can constrain D_* , R_{csm} , and ϵ_p to within a factor of ~ 10 or to a precision of $\sim 20\%$, depending on the assumed values of D_* and R_{csm} . These neutrino signals thus provide a complementary probe of the CSM profile and shock acceleration, alongside traditional electromagnetic observations.

I. INTRODUCTION

Core-collapse supernovae (CCSNe), among the most energetic explosions in the Universe, mark the violent deaths of massive stars and are copious sources of low-energy (LE) neutrinos in the range of 10–100 MeV, produced during core collapse and proto–neutron-star cooling. These neutrinos carry direct information about the explosion mechanism, neutrino interaction and transport, and the physics of hot and dense nuclear matter [1–7]. In addition to this well-established LE neutrino signal, CCSNe have been suggested as potential sources of HE neutrinos in the TeV–PeV range [8, 9]. Several HE neutrino production mechanisms have been explored. For instance, mildly relativistic jets may be launched during core collapse and could provide sites for proton acceleration at shocks as well as HE neutrino production [10–30]. An alternative scenario involves rapidly rotating compact remnants, the nascent pulsars or magnetars, which can drive relativistic winds that accelerate charged particles and generate HE neutrinos via inelastic pp scatterings when the accelerated protons collide with the expanding SN ejecta [31–34].

Another scenario involves interactions between the SN ejecta and the CSM surrounding the progenitor. As the ejecta collide with the CSM, strong collisionless shocks develop and can accelerate protons to high energies. Inelastic pp collisions between the accelerated protons and the CSM then produce charged pions and kaons, whose decays yield HE neutrinos [35]. This ejecta–CSM interaction model has attracted increasing attention in recent years, as a substantial fraction of CCSNe are inferred to undergo enhanced or eruptive mass loss shortly before explosion, leading to the formation of dense CSM around

their progenitors, as revealed by multiwavelength observations of young SNe [36, 37].

The prospect of detecting HE neutrinos from interacting SNe has been addressed in numerous studies. Early studies demonstrated that Type IIn SNe with extremely dense CSM could produce multi-TeV neutrinos detectable within $\sim 20\text{--}30$ Mpc by current neutrino telescopes [35]. Subsequent studies modeled the time-dependent SN–CSM interaction and suggested that Type IIn SNe could contribute significantly to the diffuse HE neutrino background [38, 39]. The interaction scenario was later extended to other SN types, including Type IIP, IIL, and Ibc, which have less dense but still substantial CSM, implying that the neutrino signals from SNe in the Milky Way and nearby galaxies could be observable [40, 41]. More recent efforts have focused on specific events, such as the nearby Type II SN 2023ixf [41–45], as well as potential associations between IceCube neutrino events and interacting SNe, including SN 2023uqf [46] and the Type IIn SNe 2023syz and 2025cbj [47, 48].

Most existing studies of HE neutrino emission from the SN ejecta–CSM interactions adopt specific or benchmark choices for the CSM profile and shock properties, whereas a systematic exploration of a wide range of physically plausible parameters remains limited. In particular, the dependence of neutrino signals on key physical ingredients—such as the CSM density normalization, radial extent and slope, and the microphysics of collisionless shocks including particle acceleration and magnetic-field amplification—has not been thoroughly investigated. More importantly, the inverse problem, i.e., whether neutrino observations themselves could provide meaningful constraints on the CSM structure or shock physics, remains largely unexplored.

Motivated by these considerations, we study HE neutrino emission from nearby CCSNe, explicitly accounting for the physically allowed ranges of key parameters. This approach captures the diversity of SN populations and allows us to assess how variations in CSM prop-

* Corresponding author: guogang@cug.edu.cn

erties and shock microphysics shape the resulting neutrino spectra, light curves, and event rates. Although the Galactic CCSN rate is modest (~ 1 – 3 per century [49, 50]), a nearby event could produce tens to hundreds of TeV–PeV neutrino events, enabling detailed temporal and spectral analyses. For a future Galactic Type II SN, we explore the potential of HE neutrino signals as complementary probes of both the CSM density profile and the physics of collisionless shocks, incorporating parameter uncertainties.

The structure of this paper is as follows. In Sec. II, we introduce the profiles of the SN ejecta and the CSM, including the distribution of mass-loss rates inferred from observations. We then review neutrino production in the SN ejecta–CSM interaction model, compute the resulting HE neutrino fluxes, and discuss their dependence on the relevant physical parameters. In Sec. III, we examine the detection prospects of these HE neutrinos, both from individual nearby SNe and from the cumulative diffuse flux. In the case of a Galactic SN with high event statistics, we explore in Sec. IV the potential of using neutrino observations to constrain the CSM density profile and shock acceleration. Finally, we summarize our conclusions in Sec. V.

II. BASIC FORMALISMS

A. the profiles of SN ejecta and the CSM

In this work, we focus on Type II SNe with hydrogen-rich envelope. We assume that the kinetic energy of the SN ejecta interacting with the CSM is $\mathcal{E}_{\text{ej}} = 10^{51}$ erg, and the ejecta mass is $M_{\text{ej}} = 10M_{\odot} \approx 1.989 \times 10^{34}$ g. Numerical simulations of SN explosions indicate that the SN ejecta is divided into an inner part ($\rho_{\text{ej}} \propto r^{-\delta}$) and an outer part ($\rho_{\text{ej}} \propto r^{-n}$) [51], where δ and n are the slope parameters. The outer slope depends on the progenitor structure and typically lies in the range $n \approx 10$ – 12 for CCSNe, while the density of the inner core is nearly flat with $\delta \sim 0$ – 1 [52].

Up to a characteristic radius R_{csm} , the CSM density can be described by

$$\rho_{\text{csm}}(r) = Dr^{-w}, \quad (1)$$

where w is the density slope. Throughout this work, we focus on the wind-like case with $w = 2$, while keeping the explicit dependence on w in the general expressions below. In this case, the parameter D is constant and directly related to the steady mass-loss history of the progenitor prior to core collapse,

$$D = \frac{\dot{M}}{4\pi V_{\text{w}}}, \quad (2)$$

where \dot{M} is the mass loss rate and V_{w} the wind velocity. Following Ref. [40], we introduce the dimensionless

parameter

$$D_* \equiv \frac{D}{5 \times 10^{16} \text{ g cm}^{-1}} \approx \frac{\dot{M}}{0.1 M_{\odot} \text{ yr}^{-1}} \frac{100 \text{ km s}^{-1}}{V_{\text{w}}}, \quad (3)$$

to quantify the magnitude of the CSM density. For representative values $\dot{M} = 0.1 M_{\odot} \text{ yr}^{-1}$ and $V_{\text{w}} = 100 \text{ km s}^{-1}$, we obtain $D_* \approx 1$.

The values of D_* span several orders of magnitude across different SN subclasses, reflecting large diversity of mass-loss histories shortly prior to SN explosion. Observationally, the properties of the CSM—including its density, velocity, as well as its radial extent—are inferred using a combination of diagnostics, such as early-time spectroscopy, persistent narrow emission lines, optical and ultraviolet excess emission, light-curve rise times and shapes, as well as radio and x-ray observations. Type IIn SNe are characterized by persistent narrow hydrogen emission lines, which directly trace slow-moving, dense CSM photoionized or shock-heated by the SN explosion. These features, together with luminous and slowly evolving light curves, indicate sustained and strong interaction between the SN ejecta with an extended, dense CSM. Modeling of the optical spectra, bolometric light curves, and x-ray emission typically requires high progenitor mass-loss rates of $\dot{M} \sim 10^{-3}$ – $1 M_{\odot} \text{ yr}^{-1}$ for wind velocities $V_{\text{w}} \sim 100$ – 1000 km s^{-1} , maintained over years to decades prior to core-collapse [53–59]. This corresponds to typical CSM radii $R_{\text{csm}} \sim 10^{15}$ – 10^{16} cm or larger. The resulting D_* lies in the range of 0.01– 10 assuming $V_{\text{w}} = 100 \text{ km s}^{-1}$. In contrast, red supergiant (RSG) progenitors of regular Type II SNe are generally inferred to have much lower steady mass-loss rates, $\dot{M} \sim 10^{-6}$ – $10^{-5} M_{\odot} \text{ yr}^{-1}$, when averaged over long timescales [53]. However, an increasing number of early-time optical, ultraviolet, millimeter and flash-spectroscopy observations now consistently indicates that a significant fraction of regular Type II SNe (mainly IIP and IIL) undergo short-lived episodes of strongly enhanced mass loss in the final months to \sim year before explosion (see, e.g., [37, 60–69]). These eruptive episodes can reach mass-loss rates comparable to those inferred for Type IIn SNe. However, because they are short-lived, the resulting dense CSM is confined to compact radii, $R_{\text{csm}} \sim 10^{14}$ – 10^{15} cm . Detailed analyses of recent nearby events, such as SNe 2020fqv, 2023ixf, and 2024ggi, similarly point to very large values of \dot{M} and compact CSM extents of order a few $\times 10^{14} \text{ cm}$ [70–73]. For normal Type II SNe, we only focus on the confined dense CSM produced during these eruptive mass-loss phases, which are expected to yield significantly enhanced HE neutrino fluxes.

In many previous studies, a single representative value of D_* was typically adopted for each SN subtype. For instance, canonical values such as $D_* \sim 1$ for Type IIn SNe have been used to model HE neutrino emission [40, 41, 57]. To better capture the intrinsic diversity in progenitor mass-loss histories across SN populations, we

instead adopt a more realistic approach by incorporating observationally inferred distributions of M/V_w . The inclusion of these empirical distributions allows us to statistically evaluate the discovery potential of HE neutrinos from nearby SNe and to estimate the diffuse HE neutrino background from all similar populations.

Figure 1 shows the distributions of M/V_w , or equivalently, D_* [see Eq. (3)], adopted in this study for normal Type II (excluding Type IIn¹; left) and Type IIn (right) SNe. For normal Type II SNe, we use the distribution derived from early optical observations of a magnitude-limited sample of 639 Type II SNe from the Zwicky Transient Facility [69] (see their Fig. 11 for the inferred \dot{M} , with V_w fixed at 10 km s^{-1}). For Type IIn SNe, we adopt a bimodal Gaussian distribution that fits the inferred values of M/V_w obtained from systematic light-curve modeling of a sample of 57 Type IIn SNe [58] (see their Fig. 15). Since Type IIn SNe are much rarer than normal Type II SNe, we also show weighted distributions that account for the relative fractions of the two subtypes (90% or 95% for normal Type II and the remaining 10% or 5% for Type IIn) for illustration. Notably, we find that the regular Type II SNe contribute predominantly even at the highest M/V_w values.

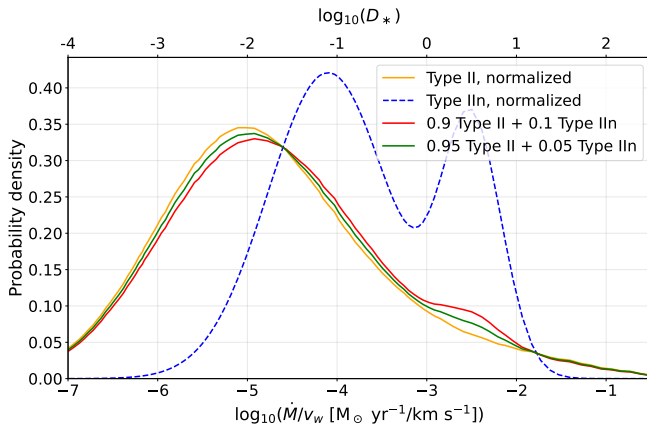


FIG. 1. Normalized (to unity) distributions of \dot{M}/V_w , or equivalently, D_* [see Eq. (3)], for regular Type II (solid orange) and Type IIn (dashed blue) SNe. Assuming relative fractions of 90% (95%) for Type II and 10% (5%) for Type IIn, the corresponding weighted distribution combining both subtypes is shown by the red (green) curve.

In addition to D_* , the CSM outer radius R_{csm} plays a crucial role in shaping the HE neutrino signal. As discussed above, the CSM surrounding normal Type II SNe is typically much more compact than that associated with Type IIn SNe. Accordingly, we consider R_{csm} in the range $10^{14}\text{--}10^{15} \text{ cm}$ for normal Type II SNe. For Type IIn SNe, we consider more extended CSM configurations with R_{csm} spanning $10^{15}\text{--}10^{17} \text{ cm}$. Throughout

this work, we adopt $R_* = 6 \times 10^{13} \text{ cm}$, $M_{\text{ej}} = 10M_\odot$, $\mathcal{E}_{\text{ej}} = 10^{51} \text{ erg}$, $n = 10$, and $\delta = 0$, unless otherwise stated.

B. neutrino production by ejecta–CSM interaction

We closely follow the formalism of Ref. [74] to compute neutrino fluxes from the SN ejecta–CSM interactions. For completeness, we briefly summarize below the key expressions relevant to neutrino production and refer the reader to Ref. [74] for further details.

The interaction between the SN ejecta and the surrounding CSM produces a thin shocked shell, bounded by a forward shock propagating into the CSM and a reverse shock propagating into the ejecta [52, 75–77]. We focus on particle acceleration and HE neutrino production at the forward shock, which is expected to dominate the emission [78].

The radius of the shocked shell evolves as [74]

$$R_s(t) = \begin{cases} R_* + \left[\frac{(3-w)(4-w)g_n}{(n-4)(n-3)D} \right]^{\frac{1}{n-w}} t^{\frac{n-3}{n-w}}, & t \leq t_{\text{dec}}, \\ R_{\text{dec}} \left(\frac{t}{t_{\text{dec}}} \right)^\lambda, & t > t_{\text{dec}}, \end{cases} \quad (4)$$

where

$$g_n = \frac{1}{4\pi n} \frac{[10(n-5)\mathcal{E}_{\text{ej}}]^{(n-3)/2}}{[3(n-3)M_{\text{ej}}]^{(n-5)/2}}, \quad (5)$$

and R_{dec} is the deceleration radius at which the swept-up CSM mass becomes comparable to the ejecta mass,

$$R_{\text{dec}} \simeq \left[\frac{(3-w)M_{\text{ej}}}{4\pi D} \right]^{\frac{1}{3-w}}. \quad (6)$$

Imposing continuity, the deceleration time t_{dec} is determined by the condition $R_{\text{dec}} = R_s(t_{\text{dec}})$.

Once $R_s > R_{\text{dec}}$, the system enters the blast-wave phase. In the adiabatic regime, the shock radius evolves as $R_s \propto t^\lambda$ with $\lambda = 2/(5-w)$, corresponding to the Sedov–Taylor solution [78, 79]. If radiative cooling is efficient, the evolution instead follows a shallower, momentum-conserving scaling with $\lambda = 1/(4-w)$ [52, 79]. As shown below, for the parameter space explored, the forward shock is generally expected to be radiative [52]. We therefore adopt the radiative blast-wave evolution throughout this study. We have also verified that adopting the adiabatic evolution instead leads to a negligible impact on the resulting neutrino signal.

The shock velocity v_s is obtained by differentiating R_s with respect to t . Because R_s follows different temporal scalings below and above R_{dec} , a direct differentiation of Eq. (4) would introduce an artificial discontinuity in V_s at $t = t_{\text{dec}}$. To avoid this unphysical behavior, we adopt an

¹ Unless stated otherwise, the term “Type II” in this work refers exclusively to regular Type II SNe, excluding Type IIn events.

empirical interpolation that smoothly connects the two asymptotic regimes,

$$V_s(t) = \bar{V}_s(t) \left(1 + \frac{\eta t}{t_{\text{dec}}}\right)^{-\Delta}, \quad (7)$$

where

$$\bar{V}_s(t) = \frac{n-3}{n-w} \left[\frac{(3-w)(4-w)g_n}{(n-4)(n-3)D} \right]^{\frac{1}{n-w}} t^{\frac{w-3}{n-w}}, \quad (8)$$

corresponds to the self-similar solution prior to deceleration. We choose $\Delta = \frac{n-3}{n-w} - \lambda$ and adopt $\eta \approx 4$, such that the late-time behavior at $t \gg t_{\text{dec}}$ smoothly approaches, to good accuracy, the shock velocity obtained by differentiating R_s in Eq. (4).

The shock transitions to a collisionless regime above the breakout radius R_{bo} , where the optical depth satisfies

$$\tau(R_{\text{bo}}) \equiv \kappa_{\text{es}} \int_{R_{\text{bo}}}^{R_{\text{csm}}} \rho_{\text{csm}}(r) dr = \frac{c}{V_s(R_{\text{bo}})}, \quad (9)$$

with $\kappa_{\text{es}} \sim 0.34 \text{ cm}^2 \text{ g}^{-1}$ being the electron-scattering opacity for a CSM of solar composition [74], and c the speed of light. If $\tau(R_*) \leq 1$ at the stellar surface, then the breakout radius coincides with the stellar radius, $R_{\text{bo}} = R_*$. Once the shock becomes collisionless, proton acceleration via the Fermi mechanism becomes efficient. The breakout radius therefore marks the onset of neutrino emission at time t_{bo} , defined by $R_s(t_{\text{bo}}) = R_{\text{bo}}$, and the emission continues until the shock reaches the outer edge of the CSM at time t_{csm} , where $R_s(t_{\text{csm}}) = R_{\text{csm}}$.

The evolution of accelerated protons between R_{bo} and R_{csm} is described by [39, 74]

$$\frac{\partial N_p(\gamma_p, r)}{\partial r} - \frac{\partial}{\partial \gamma_p} \left[\frac{\gamma_p}{r} N_p(\gamma_p, r) \right] + \frac{N_p(\gamma_p, r)}{V_s(r) t_{pp}(r)} = Q_p(\gamma_p, r), \quad (10)$$

where $N_p(\gamma_p, r)$ denotes the total number of protons in the thin shocked shell with Lorentz factors between γ_p and $\gamma_p + d\gamma_p$ at radius r . The second term accounts for adiabatic energy losses due to shell expansion, while the third term represents proton losses from inelastic pp collision, characterized by a timescale t_{pp} . As indicated in the equation, we assume a constant pp cross section, such that t_{pp} is independent of γ_p . The source term Q_p term denotes the injection rate of shock-accelerated protons as the forward shock sweeps up the CSM. The formal solution of Eq. (10) can be written in integral form:

$$N_p(\gamma_p, r) = \int_{R_{\text{bo}}}^r \frac{s}{r} e^{-\int_s^r [V_s(u) t_{pp}(u)]^{-1} du} Q_p \left(\frac{s \gamma_p}{r}, s \right) ds. \quad (11)$$

Assuming that a fraction ϵ_p of the dissipated kinetic energy is converted into the acceleration of protons, and adopting a power-law spectrum with index $p = 2$, the

injection rate Q_p (in unit of cm^{-1}) can be expressed as [47, 74]:

$$Q_p(\gamma_p, r) = \frac{9\pi\epsilon_p r^2 \rho_{\text{csm}}(r) V_s^2(r)}{8 \ln(\gamma_{p,\text{max}}/\gamma_{p,\text{min}}) m_p c^2} \gamma_p^{-2}, \quad (12)$$

where $\gamma_{p,\text{min}}$ and $\gamma_{p,\text{max}}$ are the minimal and maximal Lorentz factors of the accelerated protons at each radius. We take $\gamma_{p,\text{min}} = 1$ and determine $\gamma_{p,\text{max}}$ by comparing the proton acceleration and cooling timescales at each radius. The proton acceleration timescale is $t_{\text{acc}} \sim 6\gamma_p m_p c^3/(eBV_s^2)$, where $B = (9\pi\epsilon_B V_s^2 \rho_{\text{csm}})^{1/2}$ and ϵ_B is the fraction of energy dissipated into magnetic field. The total cooling timescale can be written as $t_{\text{tot}}^{-1} = t_{pp}^{-1} + \max[t_{\text{dyn}}^{-1}, t_{\text{cool}}^{-1}]$, where the cooling due to pp collision can be approximated as $t_{pp} \simeq (4\kappa_{pp}\sigma_{pp}c\rho_{\text{csm}}/m_p)^{-1}$ with $\kappa_{pp} \simeq 1$ and $\sigma_{pp} \simeq 3 \times 10^{-26} \text{ cm}^{-2}$, the dynamic timescale is $t_{\text{dyn}} \sim r/V_s$, and t_{cool} denotes the radiative cooling timescale [see Eq. (10) of [74]]. As the shock operates at large radii, synchrotron cooling can be safely neglected.

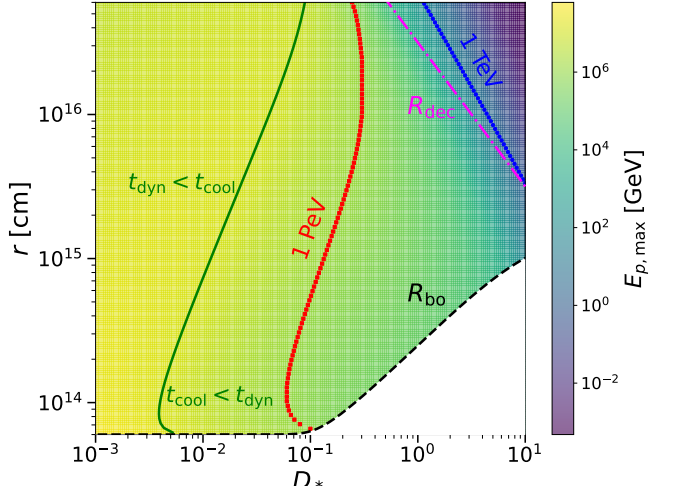


FIG. 2. Maximal attainable proton energy $E_{p,\text{max}}$ as a function of D_* and r . The contours corresponding to $E_{p,\text{max}} = 1 \text{ TeV}$ and $E_{p,\text{max}} = 1 \text{ PeV}$ are shown by the blue and red lines, respectively. The green line indicates the condition $t_{\text{dyn}} = t_{\text{cool}}$, with $t_{\text{dyn}} < t_{\text{cool}}$ ($t_{\text{cool}} < t_{\text{dyn}}$) to the left (right) of the line. Also shown are the breakout radius R_{bo} (black dashed) and the deceleration radius R_{dec} (magenta dash-dotted), both varying with D_* . Note that $R_{\text{csm}} = 10^{16} \text{ cm}$ is adopted when computing R_{bo} using Eq. (9).

Figure 2 shows the maximal attainable proton energy $E_{p,\text{max}} \equiv \gamma_{p,\text{max}} m_p c^2$ as a function of D_* and radius r , adopting $\epsilon_B = 0.1$. In realistic situations, the radius should be bounded by R_{csm} ; here, for illustration, we assume that the CSM extends to all radii shown in the figure with a wind density profile. As D_* increases, both t_{cool} and t_{pp} decrease, while t_{dyn} increases slowly as $t_{\text{dyn}} \propto D_*^{1/8}$ below R_{dec} . Overall, proton cooling is dominated by dynamical expansion, radiative losses, and

pp interactions at small, intermediate, and large D_* , respectively. The contour corresponding to $t_{\text{dyn}} = t_{\text{cool}}$ is explicitly shown by the green line, to the left (right) of which t_{dyn} (t_{cool}) dominates. At large D_* , the total cooling rate increases with D_* , thereby limiting the attainable value of $E_{p,\text{max}}$. This is clearly illustrated by the contours of $E_{p,\text{max}} = 1 \text{ TeV}$ (blue) and $E_{p,\text{max}} = 1 \text{ PeV}$ (red). For $E_{p,\text{max}} = 1 \text{ TeV}$ (1 PeV), the maximal energy is primarily determined by the competition between t_{pp} (t_{cool}) and the acceleration timescale t_{acc} .

We also show the breakout radius R_{bo} (black dashed) and the deceleration radius R_{dec} (magenta dash-dotted) as functions of D_* , calculated using Eqs. (9) and Eq. (6), respectively. In determining R_{bo} , the upper bound in Eq. (9) is fixed to $R_{\text{csm}} = 10^{16} \text{ cm}$. As seen, $t_{\text{cool}} < t_{\text{dyn}}$ at $R \gtrsim R_{\text{dec}}$, indicating that the shocked shell is likely radiative during the blast-wave phase. Note that the blast-wave phase occupies only a limited region of the D_*-r parameter space and therefore plays a minor role in this study.

Once $N_p(\gamma_p, r)$ is obtained, the all-flavor, energy-differential neutrino emissivity (in units of $\text{GeV}^{-1} \text{ s}^{-1}$) from pp collisions can be expressed as

$$I_\nu(E_\nu, t) \equiv \frac{dN_\nu}{dE_\nu dt} = \int_{\gamma_{p,\text{min}}}^{\gamma_{p,\text{max}}} N_p(\gamma_p, R_s(t)) \frac{4\rho_{\text{csm}}(r)\sigma_{pp}c}{m_p} \times Y_\nu(E_p = \gamma_p m_p c^2, E_\nu) d\gamma_p, \quad (13)$$

where $Y_\nu(E_p, E_\nu)$ is the averaged neutrino spectrum produced per pp collision. To obtain Y_ν , we employ PYTHIA 8.3 [80] to simulate the production of π^\pm and K^\pm , and to compute the resulting HE neutrino spectra by accounting for the decays of π^\pm and K^\pm , and the subsequent decay of μ^\pm , following the procedures described in Refs. [28, 81, 82]. The cooling of mesons can be safely neglected under the conditions considered here. The total neutrino spectrum emitted over a given time interval $[t_1, t_2]$ is then obtained by integrating the time-dependent emissivity over that period.

As commonly adopted in the literature [40], the neutrino flux can be estimated without explicitly solving the proton transport equation. In this simplified approach, a fraction f_{pp} of the injected protons is assumed to interact inelastically with the ambient medium to produce HE neutrinos through pp collisions. The resulting neutrino emissivity can then be expressed as

$$I_\nu^0(E_\nu, t) \simeq \int d\gamma_p Q_p(\gamma_p, R_s(t)) f_{pp}(t) Y_\nu(E_p, E_\nu), \quad (14)$$

where $E_p = \gamma_p m_p c^2$ and the effective interaction probability is approximated as $f_{pp}(t) \sim \min[t_{\text{dyn}}/t_{pp}, 1] \sim \min[\sigma_{pp}(4\rho_{\text{csm}}/m_p)R_s(t)c/V_s(t), 1]$.

C. the resulting neutrino fluxes

As seen, the neutrino fluence from the interaction of the SN ejecta with the CSM is governed by a set of physical parameters. To illustrate the results in this section,

we adopt the following fiducial values unless otherwise specified: $D_* = 0.01$ or 1 , $R_{\text{csm}} = 10^{15} \text{ cm}$, $\epsilon_B = 0.1$, and $\epsilon_p = 0.1$.

The resulting neutrino flux from a nearby SN located at 10 kpc and its dependence on a few relevant parameters, including D_* , R_{csm} , ϵ_B , n and δ , are presented in Fig. 3. The upper left panel shows the significant influence of D_* on the neutrino flux. A wide range of D_* values, $D_* = 10^{-4}, 10^{-3}, 10^{-2}, 0.1, 1, 10$, is considered. As expected, lower D_* values result in a reduced overall flux normalization but a higher cutoff energy in the neutrino spectrum. This can be understood as follows: a lower CSM density reduces both the amount of swept-up CSM and the rate of pp collisions, thereby decreasing the flux, but it also increases the pp cooling timescale. Consequently, protons can be accelerated to higher energies before interacting, raising the maximum proton energy and shifting the neutrino spectrum cutoff to higher energies.

This panel also compares the neutrino fluxes obtained by solving the proton transport equation [thick lines, Eqs. (10) and (13)] and those calculated without solving it [thin lines, Eq. (14)]. As shown in the figure, explicitly including proton transport accounts for the cooling of HE protons toward lower energies, which suppresses their contribution to the HE neutrino flux. In contrast, the simplified treatment without proton transport assumes that the accelerated protons effectively interact with the ambient medium over a dynamical timescale t_{dyn} , without properly taking into account the cooling of protons during their evolution. We find that including proton transport can reduce the neutrino flux by a factor of ~ 2 . This effect becomes less pronounced at higher CSM densities (e.g., $D_* \gtrsim 0.1$), where the increased target density results in a shorter pp collision timescale and adiabatic cooling becomes negligible.

The upper right panel compares the neutrino flux for different values of R_{csm} (10^{14} cm , 10^{15} cm , 10^{16} cm , and 10^{17} cm), assuming $D_* = 0.01$ and 1 . A more extended CSM generally leads to a higher total neutrino flux compared to a compact configuration, owing to the larger total CSM mass swept up for pp interactions, which sustains neutrino emission over a longer duration. Despite the fact that the D_* values for both subclass can be comparable, the more compact CSM leads to lower neutrino fluxes from typical Type II SNe compared to Type IIn SNe, which possess more extended CSM. Note that the dependence on R_{csm} is not linear. As the shock propagates to larger radii, the decreasing CSM density reduces the pp interaction optical depth, leading to a saturation effect that further increases in R_{csm} result in diminishing gains in the total integrated neutrino flux.

The dominant effect of ϵ_B is on the proton acceleration timescale, $t_{\text{acc}} \propto E_p/B \propto E_p \epsilon_B^{-1/2}$. As all the relevant cooling time scales, t_{dyn} , t_{cool} , and t_{pp} , are independent of E_p , the balance between the cooling and acceleration timescales implies $E_{p,\text{max}} \propto \epsilon_B^{1/2}$. As a result, the neutrino spectrum extends to higher energies with increasing

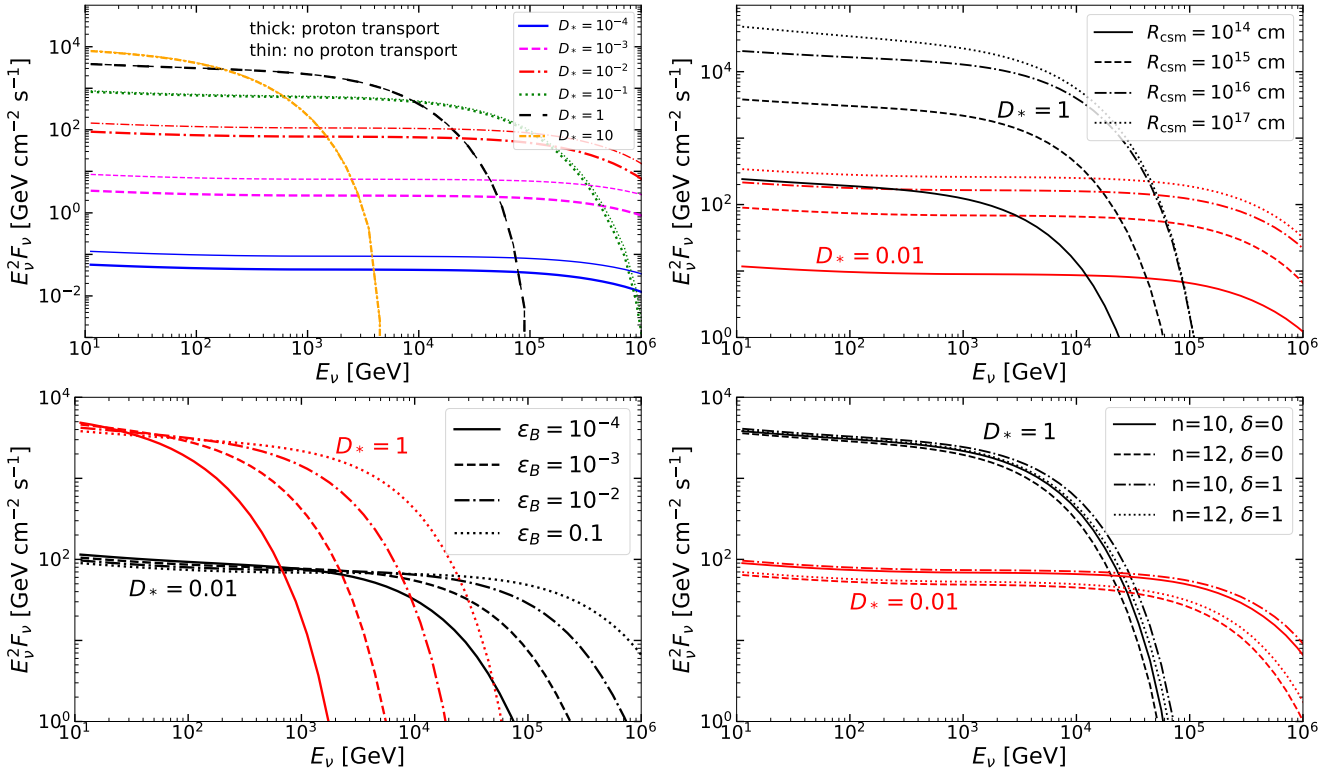


FIG. 3. Expected all-flavor neutrino fluxes from a nearby CCSN at $L = 10$ kpc using different values of D_* (upper left), R_{csm} (upper right), ϵ_B (lower left), and n and δ (lower right). In the upper panel, neutrino fluxes calculated with (thick) or without (thin) solving the proton transport equation are also compared. We adopt $D_* = 0.01$ or 1 , $R_{\text{csm}} = 10^{15}$ cm, $\epsilon_B = 0.1$, and $\epsilon_p = 0.1$, unless otherwise specified.

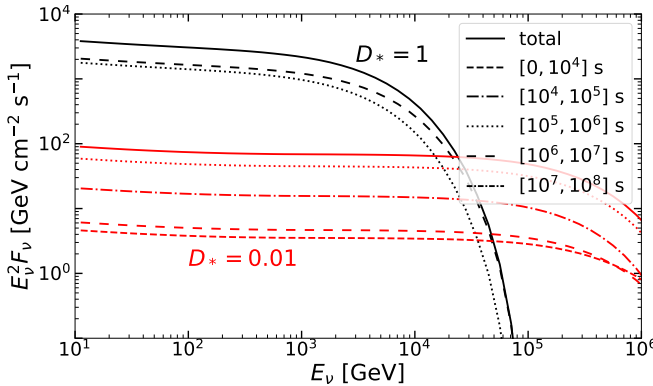


FIG. 4. Expected all-flavor neutrino fluxes from a nearby SN at $L = 10$ kpc with $D_* = 0.01$ and 1 . Five different time windows after the explosion have been considered. The same parameter values as in Fig. 3 are taken.

ϵ_B (see the lower left panel of Fig. 3 for $\epsilon_B = 10^{-4}$, 10^{-3} , 10^{-2} , and 0.1).

The parameters n and δ , which characterize the SN ejecta structure, have only a relatively minor impact on the neutrino flux, primarily affecting its overall normalization. As shown in the lower right panel of Fig. 3, variations within typical ranges ($n = 10$ – 12 and $\delta = 0$ – 1)

lead to changes of up to ± 20 – 30% . In the following studies, we simply fix $n = 10$ and $\delta = 0$. Although not shown, the neutrino flux scales linearly with ϵ_p . Since the effects of n and δ effectively act as a normalization uncertainty, they can be absorbed into ϵ_p , whose uncertainty will be taken into account.

It is worthy noting that different combinations of parameters can produce similar neutrino fluxes. For example, both D_* and ϵ_B influence the neutrino spectrum: ϵ_B primarily affects the maximum proton energy (and thus the spectral cutoff), while D_* impacts both the cutoff and the overall flux normalization. Different combinations of D_* and ϵ_B , with appropriate tuning of ϵ_p , can therefore produce similar neutrino signals. The temporal evolution of the neutrino signal can help break these parameter degeneracies, since D_* effectively controls the emission duration. Fig. 4 shows the expected neutrino flux within successive time windows: $[0, 10^4]$ s, $[10^4, 10^5]$ s, $[10^5, 10^6]$ s, $[10^6, 10^7]$ s, and $[10^7, 10^8]$ s. As more CSM is swept up at later times, these windows generally contribute more strongly to the total signal, particularly at lower energies. However, for low D_* values (e.g., $D_* = 0.01$), the CSM density at large radii becomes sufficiently low that the pp interaction probability is significantly suppressed, causing the windows of $[10^6, 10^7]$ s and $[10^7, 10^8]$ s to contribute less than the earlier inter-

val. For large D_* (e.g., $D_* = 1$), the shock breakouts at large R_{bo} (see Fig. 2), and as a result, neutrino emission begins at later times.

III. DETECTION PROSPECTS FOR A NEARBY SN AND THE DIFFUSE FLUX

The mass-loss rate distributions and neutrino fluxes derived in Sec. II serve as the astrophysical inputs for evaluating the detectability of these neutrino signals. Based on these results, we first examine the detection prospects of HE neutrinos from a nearby SN, adopting representative values of D_* and R_{csm} for Type II and Type IIn SNe. We then compute the resulting diffuse neutrino flux from these two subclasses, accounting for the distribution of D_* .

Unless otherwise specified, we adopt $D_* = 0.01$ and $R_{\text{csm}} = 4 \times 10^{14} \text{ cm}$ for Type II SNe [37, 61, 69], and $D_* = 1$ and $R_{\text{csm}} = 10^{16} \text{ cm}$ for Type IIn SNe [59], both located at a distances of 10 kpc. We further set $\epsilon_p = 0.1$ and consider different values of ϵ_B ranging from 10^{-4} –0.1. These benchmark parameter values are summarized in Table I. When estimating the cumulative diffuse flux, we employ the observationally inferred D_* distributions, while adopting the benchmark values of R_{csm} for each subclass and ϵ_p .

TABLE I. Benchmark parameter values adopted for Type II and Type IIn SNe in our study of the detection prospects for neutrino signals from a nearby SN. We fix the remaining parameters to $R_* = 6 \times 10^{13} \text{ cm}$, $M_{\text{ej}} = 10 M_\odot$, $\mathcal{E}_{\text{ej}} = 10^{51} \text{ erg}$, $n = 10$, and $\delta = 0$, as mentioned in Sec. II.

	D_*	R_{csm}	ϵ_B	ϵ_p
Type II	0.01	$4 \times 10^{14} \text{ cm}$	$10^{-4}, 0.1$	0.1
Type IIn	1	10^{16} cm	$10^{-4}, 0.1$	0.1

A. Detecting HE neutrinos from a nearby SN

We focus on IceCube [83] to study the neutrino signal, although the approach can be readily extended to other detectors such as ANTARES [84], KM3NeT [85], and planned next-generation telescopes [86–88]. Two primary event topologies are commonly used in searches for astrophysical neutrinos: track events, which are mainly produced by charged-current (CC) interactions of ν_μ and $\bar{\nu}_\mu$ (with a subdominant contribution from CC interactions of ν_τ and $\bar{\nu}_\tau$ through tau decays), and cascade events, arising from CC interactions of electron and tau neutrinos as well as neutral-current interactions of all flavors. Owing to their substantially larger effective area and superior angular resolution, track events play a key role in searches for neutrinos from astrophysical sources (see, e.g., [89–94]). Note that atmospheric muons constitute a

major background for downgoing track events, while for upgoing tracks, this contamination is strongly suppressed by the shielding effect of the Earth. To detect HE neutrinos from the Southern Hemisphere with IceCube, cascade events—especially starting cascades—are better suited, as they efficiently reject the atmospheric muon background [95–97]. For illustration, we restrict our analysis to upgoing track events, corresponding to sources located in the Northern Hemisphere. We note, however, that the inclusion of starting cascade events could yield comparable detection prospects for Northern Hemisphere sources, as demonstrated in Ref. [82].

To quantitatively assess the discovery potential of HE neutrinos from nearby SNe, we perform a binned likelihood analysis similar to that adopted in Ref. [82]. We always assume that the source distance L is well known², and that a given SN ejecta-CSM interaction model can be characterized by the parameter set

$$\boldsymbol{\lambda} \equiv \{D_*, R_{\text{csm}}, \epsilon_B, \epsilon_p\}. \quad (15)$$

The expected number of track events induced by neutrinos in each time and energy bin is then given by

$$s_{ij}(\boldsymbol{\lambda}) = \sum_{f=\nu_\mu, \bar{\nu}_\mu, \nu_\tau, \bar{\nu}_\tau} \int_{t_i^{\text{low}}}^{t_i^{\text{up}}} dt \int dE_\nu F_f(E_\nu, t) A_{f,j}(E_\nu, \theta), \quad (16)$$

where $t_i^{\text{low}, \text{up}}$ are the lower and upper bounds of the i -th time bin, $F_f(E_\nu, t)$ (in unit of $\text{GeV}^{-1} \text{ cm}^{-2} \text{ s}^{-1}$) is the time-dependent neutrino flux at Earth for flavor f , and $A_{f,j}(E_\nu, \theta)$ is the IceCube effective area for a neutrino of flavor f to produce a track event with deposited energy E_d in the j -th energy bin, which depends on neutrino energy E_ν and zenith angle θ . For simplicity, we assume that the neutrino flux is equally distributed between neutrinos and antineutrinos, and among all flavors as a result of neutrino oscillations. For upgoing tracks, we adopt the effective areas from [89, 98]. We take five post-explosion time bins as in Fig. 4: $[0, 10^4]$ s, $[10^4, 10^5]$ s, $[10^5, 10^6]$ s, $[10^6, 10^7]$ s, and $[10^7, 10^8]$ s, and use the same energy bins for E_d as provided in the effective-area tables.

Figure 5 shows the expected track spectra at IceCube produced by HE neutrinos from a Type II (left panel) and a Type IIn (right panel) SN located at 10 kpc, adopting the benchmark parameter values listed in Table I. To illustrate the impact of the magnetic-field energy fraction, we consider $\epsilon_B = 10^{-4}$ and 0.1. In all cases, the deposited-energy spectra peak at $E_d \sim 1 \text{ TeV}$, while the suppression at higher energies is primarily caused by the absorption of HE neutrinos in the Earth. The higher event rates predicted for Type IIn SNe or for larger ϵ_B reflect the dependence of the neutrino flux on D_* , R_{csm} , ϵ_B , as discussed in Sec. II.

² The uncertainty in L can be absorbed into ϵ_p .

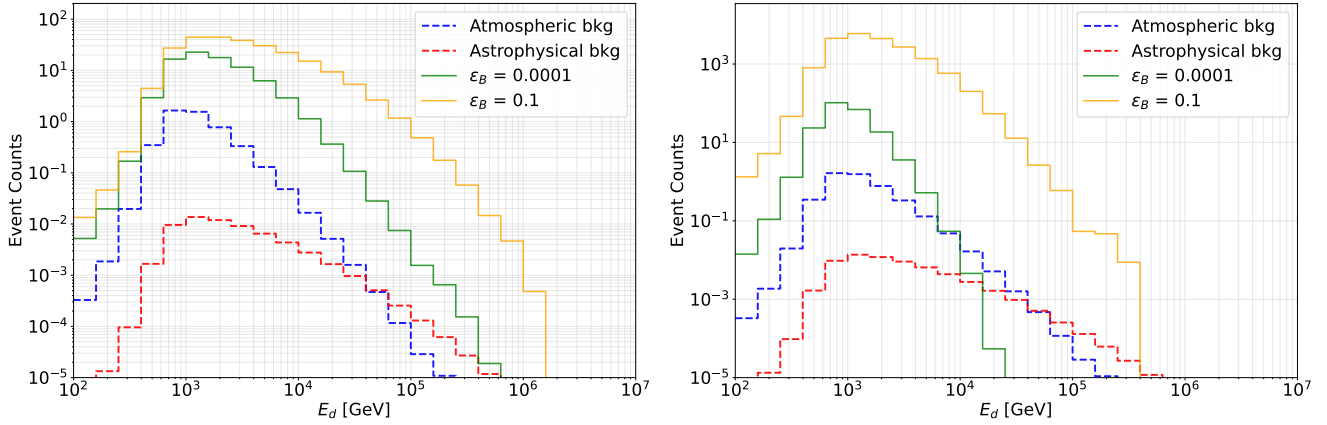


FIG. 5. Expected track spectra at IceCube from a Type II SN (left panel) with $D_* = 0.01$ and $R_{\text{csm}} = 4 \times 10^{14}$ cm, and from a Type IIn SN (right panel) with $D_* = 1$ and $R_{\text{csm}} = 10^{16}$ cm, both located at a distance of $L = 10$ kpc. Two values of $\epsilon_B = 10^{-4}$ and 0.1 are adopted. For parameters not explicitly specified, the benchmark values listed in Table I are adopted.

For comparison, we also show the expected background contributions from atmospheric neutrinos and diffuse astrophysical neutrinos, which constitute the dominant background for upgoing track events. The atmospheric component is computed using MCEq [99], while the diffuse astrophysical neutrino flux is modeled by a single power-law spectrum based on the IceCube 9.5-year track data [100]. The background rate is evaluated within a 1° angular search window around the SN direction, corresponding to a solid angle $\Delta\Omega \simeq 0.001$. With this selection, the total background amounts to ~ 3 events above 0.1 TeV, concentrated mainly at TeV energies. For a typical Galactic Type II SN, the predicted signal significantly exceeds the background over the relevant energy range, suggesting that backgrounds play only a minor role.

The likelihood function incorporating contributions from both signal and background is defined as

$$\mathcal{L}(\{s_{ij}(\boldsymbol{\lambda})\}) = \max_{\{f_b\}} \left\{ \prod_{ij} P(N_{ij}, s_{ij}(\boldsymbol{\lambda}) + (1 + f_b)b_{ij}) \times \exp \left(-\frac{f_b^2}{2\sigma_b^2} \right) \right\}, \quad (17)$$

where $P(N, \mu)$ denotes the Poisson probability of observing N events given an expectation value μ , N_{ij} is the total number of detected track events in the i -th time and j -th energy bin, and s_{ij} is the predicted signal number depending on the SN interaction model [see Eq. (16)], and b_{ij} is the expected background number. The parameter f_b is introduced as a nuisance parameter to account for the overall normalization uncertainty of the background, with an associated variance σ_b . As indicated, the likelihood function in Eq. (17) is maximized with respect to f_b . We set $\sigma_b = 0.2$, and note that the exact value does not affect the final results.

The discovery potential is quantified using the test statistic (TS), defined as the logarithmic likelihood ratio between the signal-plus-background and background

only hypotheses. Throughout this work, we compute the median discovery significance using the Asimov dataset [101]. For given SN model characterized by $\boldsymbol{\lambda}$, the observed counts N_{ij} in Eq. (17) are set equal to the expected values under the signal-plus-background hypothesis: $N_{ij} = s_{ij}(\boldsymbol{\lambda}) + b_{ij}$. Using the definition of \mathcal{L} in Eq. (17), the TS is then given by

$$\text{TS}(\boldsymbol{\lambda}) = 2[\ln \mathcal{L}(\{s_{ij}(\boldsymbol{\lambda})\}) - \ln \mathcal{L}(\{s_{ij} = 0\})]. \quad (18)$$

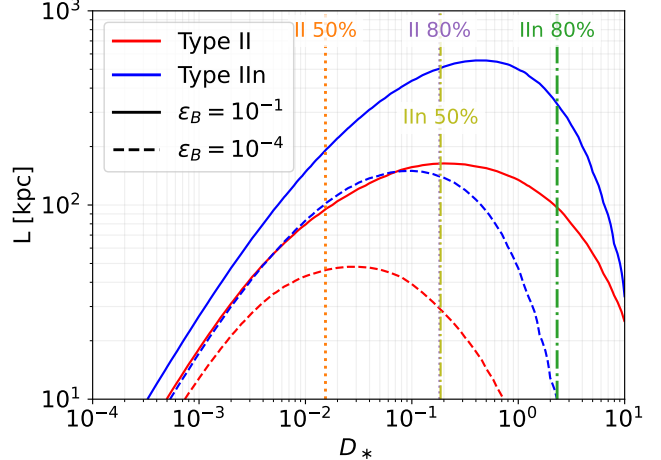


FIG. 6. Detection horizons for HE neutrinos from Type II (red) and Type IIn (blue) SNe as a function of D_* . We adopt a 3σ detection criterion, corresponding to $\text{TS} = 9$ [see Eq. (18)]. Results are shown for $R_{\text{csm}} = 4 \times 10^{14}$ cm (Type II) and $R_{\text{csm}} = 10^{16}$ cm (Type IIn), assuming $\epsilon_B = 10^{-4}$ (dashed) and 0.1 (solid). Vertical lines indicate the cumulative probabilities (50% and 80%) for Type II and Type IIn SNe to have D_* below a given value, based on the normalized mass-loss rate distributions shown in Fig. 1.

Figure 6 shows the resulting detection horizons at the 3σ confidence level (CL; $\text{TS} = 9$) as a function of D_* , assuming $R_{\text{csm}} = 4 \times 10^{14}$ cm and 10^{16} cm, and $\epsilon_B = 10^{-4}$

and 0.1. For regular Type II SNe, the detection horizon increases with D_* for $D_* \lesssim 0.03$ ($\epsilon_B = 10^{-4}$) or $D_* \lesssim 0.3$ ($\epsilon_B = 0.1$), and then decreases at larger D_* , reflecting the dependence of neutrino flux on D_* (see the upper left panel of Fig. 3). In the optimal D_* regime, the horizon extends to ~ 0.05 –0.2 Mpc, depending on ϵ_B . With a more extended CSM, the neutrino flux from Type IIn SNe exceeds that of normal Type II SNe for a given D_* . As a result, the detection horizon for Type IIn can reach ~ 0.15 Mpc for $\epsilon_B = 10^{-4}$ and ~ 0.6 Mpc for $\epsilon_B = 0.1$. The vertical lines indicate the cumulative probability contours (50% and 80%) that a Type II (red) or Type IIn (blue) SN has D_* below a given value, inferred from the observed mass-loss rate distributions. A substantial fraction of Type II and Type IIn SNe lie within their respective optimal D_* ranges, implying that a significant subset of nearby events occurs under favorable CSM conditions for HE neutrino detection. For typical Galactic Type II SNe ($L = 10$ kpc) with D_* in the range 10^{-3} –1, HE neutrino detection at $\gtrsim 3\sigma$ CL can be achieved.

These results are broadly consistent with those of Ref. [41], which similarly identified regular Type II SNe located within ~ 1 Mpc with moderately dense winds as promising sources of HE neutrinos detectable by IceCube. Note that $\epsilon_p = 0.1$ is adopted in Fig. 2. As easily understood, the detection horizon scales as $\epsilon_p^{1/2}$ for fixed D_* and ϵ_B .

B. Detection prospect for the diffuse neutrino flux

The diffuse HE neutrino flux from Type II and Type IIn SNe is obtained by integrating the neutrino fluence from individual events over redshift,

$$\Phi_{\text{diff}}(E_\nu) = \frac{c}{4\pi} \int_0^\infty R_{\text{cc}}(z) \left\langle \frac{dN_\nu}{dE_\nu}(E_\nu(1+z)) \right\rangle \times (1+z) \left| \frac{dt}{dz} \right| dz. \quad (19)$$

Here, $R_{\text{cc}}(z)$ is the total CCSN rate [102], and dt/dz denotes the cosmic time-redshift relation, evaluated following Ref. [82]. $\langle dN_\nu(E_\nu)/dE_\nu \rangle$ is the all-flavor time-integrated neutrino spectrum per CCSN (in unit of GeV^{-1}), averaged over the distribution of D_* :

$$\left\langle \frac{dN_\nu(E_\nu)}{dE_\nu} \right\rangle = \int \left[\eta_{\text{II}} f_{\text{II}}(\log_{10} D_*) \frac{dN_\nu^{(\text{II})}(E_\nu)}{dE_\nu} + \eta_{\text{IIn}} f_{\text{IIn}}(\log_{10} D_*) \frac{dN_\nu^{(\text{IIn})}(E_\nu)}{dE_\nu} \right] d\log_{10} D_*, \quad (20)$$

with $dN_\nu^{(\text{II,IIn})}(E_\nu, D_*)/dE_\nu$ being the total emitted neutrino spectra from individual Type II and Type IIn SN with a given D_* . We adopt $R_{\text{csm}} = 4 \times 10^{14}$ cm for Type II SNe and $R_{\text{csm}} = 10^{16}$ cm for Type IIn SNe, and consider their normalized D_* distributions f_{II} and f_{IIn}

(Fig. 1), weighted by the relative fractions $\eta_{\text{II}} \simeq 61.3\%$ and $\eta_{\text{IIn}} \simeq 5.7\%$ of all CCSNe inferred from recent SN observations [103]. We further fix $\epsilon_p = 0.1$ and consider $\epsilon_B = 10^{-4}$ and 0.1.

Figure 7 shows the resulting diffuse neutrino flux, including the separate contributions from Type II and Type IIn SNe, together with their sum. As discussed above, the D_* distribution of regular Type II SNe, when weighted by their relative occurrence rates, exceeds that of Type IIn SNe, even at the high- D_* end. However, typical Type II SNe are surrounded by more compact CSM. As a result, the diffuse neutrino flux is dominated by Type IIn SNe, in agreement with earlier studies [104]. Nevertheless, regular Type II SNe provide a non-negligible contribution, particularly at the highest energies.

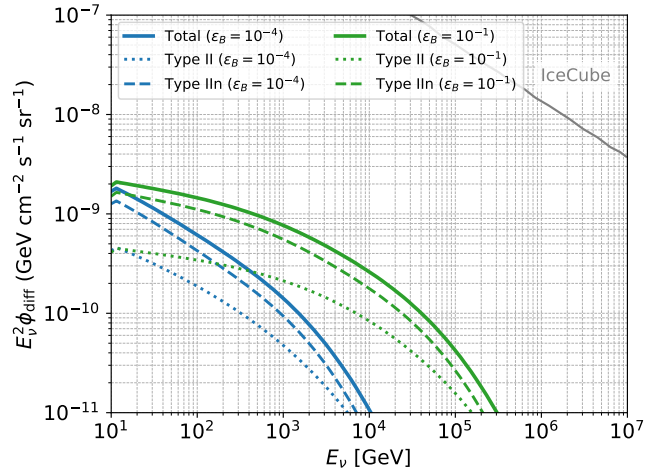


FIG. 7. Predicted diffuse HE neutrino flux from Type II and Type IIn SNe in the SN ejecta-CSM interaction model. Contributions from Type II and Type IIn SNe, as well as their sum, are shown for $\epsilon_B = 10^{-4}$ (blue) and 0.1 (green). The detected IceCube 10-year diffuse neutrino flux using starting track events [97] is shown for comparison (grey).

Even under optimistic assumptions ($\epsilon_B = 0.1$), the predicted diffuse flux arising from the SN ejecta–CSM interactions remains 2–3 orders of magnitude below the observed flux by IceCube (the grey line) [97], using the 10.3-year Enhanced Starting Track Event Selection (ESTES) dataset. The predicted flux is also consistent with the limits derived from IceCube searches for HE neutrinos from samples of known CCSNe [105]. This small diffuse contribution implies that HE neutrinos from nearby individual SNe offer more promising detection prospects.

IV. CONSTRAINING CSM AND PARTICLE ACCELERATION PARAMETERS

In the previous section, we assessed the discovery significance of HE neutrinos from a single nearby SN by adopting fixed values for the parameter set $\lambda =$

$(D_*, R_{\text{csm}}, \epsilon_B, \epsilon_p)$. In practice, however, these parameters are all highly uncertain and may vary substantially across different SN progenitors. In this section, we investigate the potential of using HE neutrino signals to constrain these parameters, incorporating their uncertainties within a consistent statistical framework.

Since the expected background rate is low, we neglect its uncertainty and define the likelihood function as

$$\mathcal{L}'(\boldsymbol{\lambda}) = \prod_{ij} P(N_{ij}, s_{ij}(\boldsymbol{\lambda}) + b_{ij}), \quad (21)$$

where all quantities are defined as in Eq. (17). To estimate the median expected sensitivity, we employ the Asimov dataset, for which the observed counts are fixed to $N_{ij} = s_{ij}(\boldsymbol{\lambda}_0) + b_{ij}$, with $\boldsymbol{\lambda}_0$ denoting a benchmark parameter set. For this dataset, the global maximum of the likelihood naturally occurs at $\boldsymbol{\lambda} = \boldsymbol{\lambda}_0$.

For illustrative purpose, we project constraints in both one- and two-dimensional parameter spaces using the above defined likelihood function. For one-dimensional constraints, a single parameter of interest is varied while the remaining three parameters are allowed to float freely within physically motivated ranges. For example, when constraining the parameter D_* , the TS is defined as

$$\text{TS}'(D_*) = 2 \left[\ln \mathcal{L}'\left(D_*, \hat{R}_{\text{csm}}, \hat{\epsilon}_B, \hat{\epsilon}_p\right) - \ln \mathcal{L}'(\boldsymbol{\lambda}_0) \right], \quad (22)$$

where \hat{R}_{csm} , $\hat{\epsilon}_B$, and $\hat{\epsilon}_p$ denote the values that maximize the likelihood for each fixed D_* . Similarly, for two-dimensional constraints, the likelihood is evaluated for a pair of parameters of interest, with the remaining two parameters profiled over. For instance, when constraining (D_*, R_{csm}) , the TS is

$$\text{TS}'(D_*, R_{\text{csm}}) = 2 \left[\ln \mathcal{L}'(D_*, R_{\text{csm}}, \hat{\epsilon}_B, \hat{\epsilon}_p) - \ln \mathcal{L}'(\boldsymbol{\lambda}_0) \right], \quad (23)$$

where $\hat{\epsilon}_B$ and $\hat{\epsilon}_p$ maximize the likelihood at each fixed (D_*, R_{csm}) . The resulting TS contours quantify the joint constraints on the parameters and reveal correlations among them.

For our analysis, the parameters are varied over typical ranges inferred from observations of Type II SNe:

$$\begin{aligned} D_* &\in [10^{-4}, 10], \quad R_{\text{csm}} \in [10^{14}, 10^{17}] \text{ cm}, \\ \epsilon_B &\in [10^{-4}, 0.1], \quad \epsilon_p \in [10^{-4}, 1]. \end{aligned}$$

Following Wilks' theorem, TS values of 9 and 25 correspond to 3σ and 5σ CLs, respectively, for one-dimensional constraints, while the corresponding values for two-dimensional constraints are $\text{TS} \approx 11.83$ and 28.74.

The two-dimensional constraints for a Type II SN at a distance of 10 kpc are shown in Fig. 8. For illustration, we adopt the benchmark values $D_* = 0.01$, $R_{\text{csm}} = 4 \times 10^{14}$ cm, $\epsilon_B = 0.01$, and $\epsilon_p = 0.1$. The most prominent correlation appears in the (D_*, ϵ_p) plane, where the

confidence contours exhibit an elongation along a diagonal direction, indicating that the combination D_*/ϵ_p is relatively well constrained over a certain parameter region. The degeneracy between D_* and ϵ_p is physically expected, as both parameters influence the overall signal strength. However, variations in D_* introduce distinct spectral and temporal features that cannot be fully reproduced by rescaling ϵ_p alone, thereby partially breaking the degeneracy once full energy- and time-dependent information is incorporated in the likelihood analysis. Comparably weaker correlations are present in the (D_*, R_{csm}) and $(R_{\text{csm}}, \epsilon_p)$ planes for similar reasons. The parameter ϵ_B mainly affects the HE cutoff of the spectrum. This effect can be partially mimicked by correlated changes in other parameters: as variations in D_* can modify the spectral shape while ϵ_p rescales the overall neutrino flux. Consequently, mild residual degeneracies arise between ϵ_B and D_* or ϵ_p . There is nearly no degeneracy between R_{csm} and ϵ_B .

As shown in the Fig. 8, for Type II SNe with $D_* = 0.01$, the parameter R_{csm} can be constrained to within a factor of $\sim 2\text{--}3$. By comparison, D_* and ϵ_p can only be constrained to within a factor of ~ 10 , while ϵ_B remains essentially unconstrained. These differences reflect the distinct roles of the model parameters in shaping the neutrino signal. The parameters D_* , R_{csm} , and ϵ_p all control the overall signal strength (see Sec. II); however, R_{csm} additionally governs the temporal evolution of the emission, in particular its duration and termination, which cannot be easily reproduced by variations of other parameters. With the inclusion of time-dependent information in the likelihood analysis, R_{csm} can therefore be relatively well constrained. In contrast, although D_* also affects the neutrino spectrum, its impact on the flux normalization and spectral cutoff can be partially mimicked by correlated variations in ϵ_p and ϵ_B . This degeneracy (see the middle left panel of Fig. 8) limits the constraining power on both D_* and ϵ_p . The parameter ϵ_B primarily influences the HE cutoff and has a comparatively modest effect on the overall signal, resulting in weaker constraints.

To account for the diversity of SN populations, we present the projected one-dimensional constraints (3σ CL) on each relevant parameter for both Type II ($R_{\text{csm}} = 4 \times 10^{14}$ cm) and Type IIn ($R_{\text{csm}} = 10^{16}$ cm) SNe at distances of 10 kpc in Figs. 9 (for D_* and R_{csm}) and 10 (for ϵ_B and ϵ_p), assuming different benchmark values of D_* . Two representative values, $\epsilon_B = 10^{-3}$ and 10^{-2} , are considered. For each parameter, the corresponding benchmark value is indicated by a diamond symbol. The comparison between the projected upper and lower bounds and the benchmark values illustrates how well each parameter can be constrained for a given benchmark model.

As D_* increases, the expected number of signal events grows, leading to progressively tighter constraints on all relevant parameters (Figs. 9 and 10). At the optimal benchmark value $D_* \sim 0.1$ for Type II SNe, D_* , R_{csm} , and ϵ_p can all be constrained to within a factor of ~ 2 , while ϵ_B can be determined to within a factor of $\sim 5\text{--}$

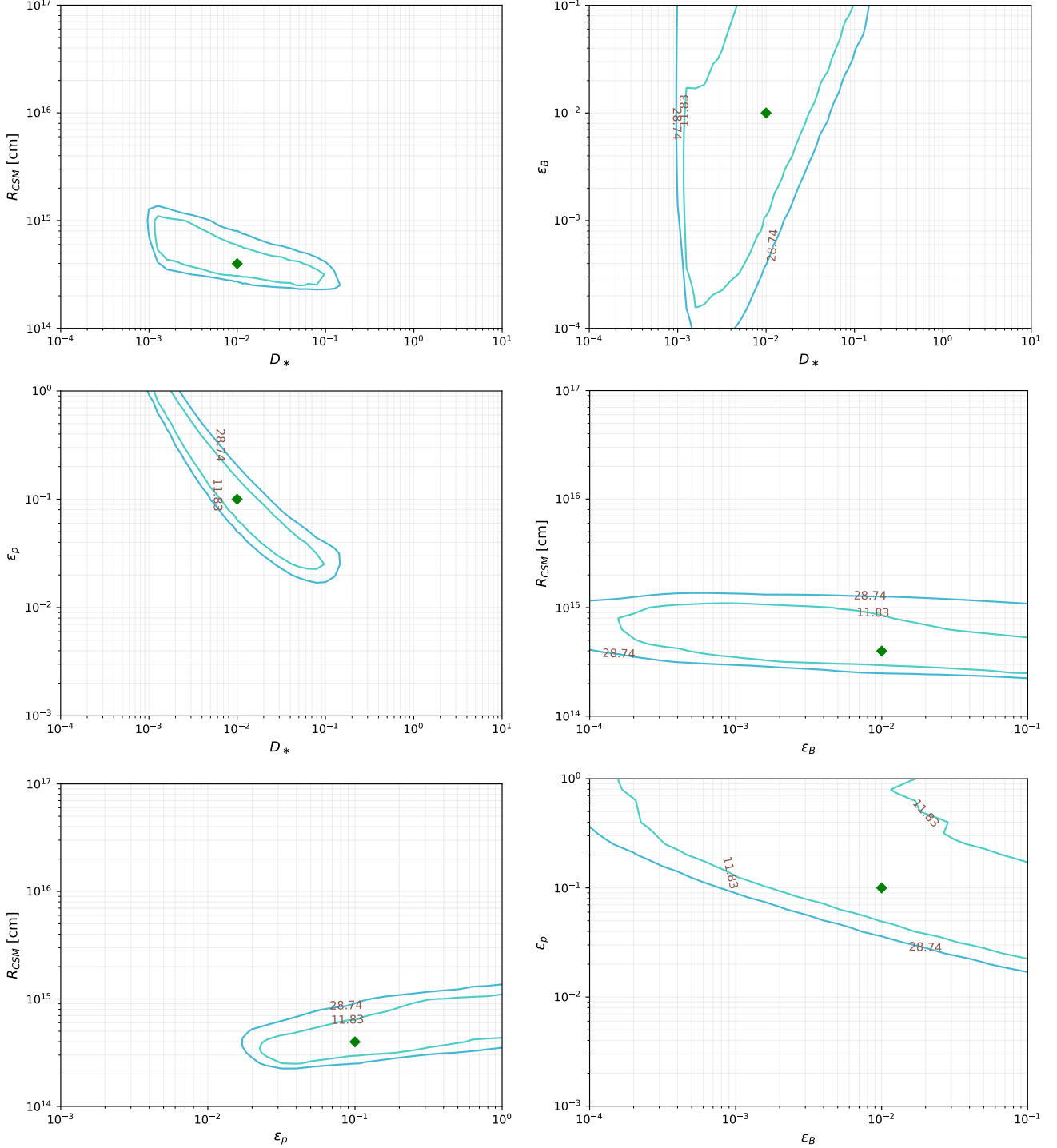


FIG. 8. Two-dimensional profile likelihood constraints on the parameters for a Galactic Type II SN at 10 kpc. Shown are 3σ ($\text{TS} = 11.83$) and 5σ ($\text{TS} = 28.74$) contours of in the planes of (D_*, R_{csm}) (upper left), (D_*, ϵ_B) (upper right), (D_*, ϵ_p) (middle left), $(\epsilon_B, R_{\text{csm}})$ (middle right), $(\epsilon_p, R_{\text{csm}})$ (lower left), and (ϵ_B, ϵ_p) (lower right). In each panel, the two parameters shown are varied while the other two parameters are profiled over. For the benchmark model, we consider a typical Type II SN located at 10 kpc with $D_* = 0.01$, $R_{\text{csm}} = 4 \times 10^{14}$ cm, $\epsilon_B = 0.01$, and $\epsilon_p = 0.1$ indicated by filled diamond symbols in the 2D parameter spaces.

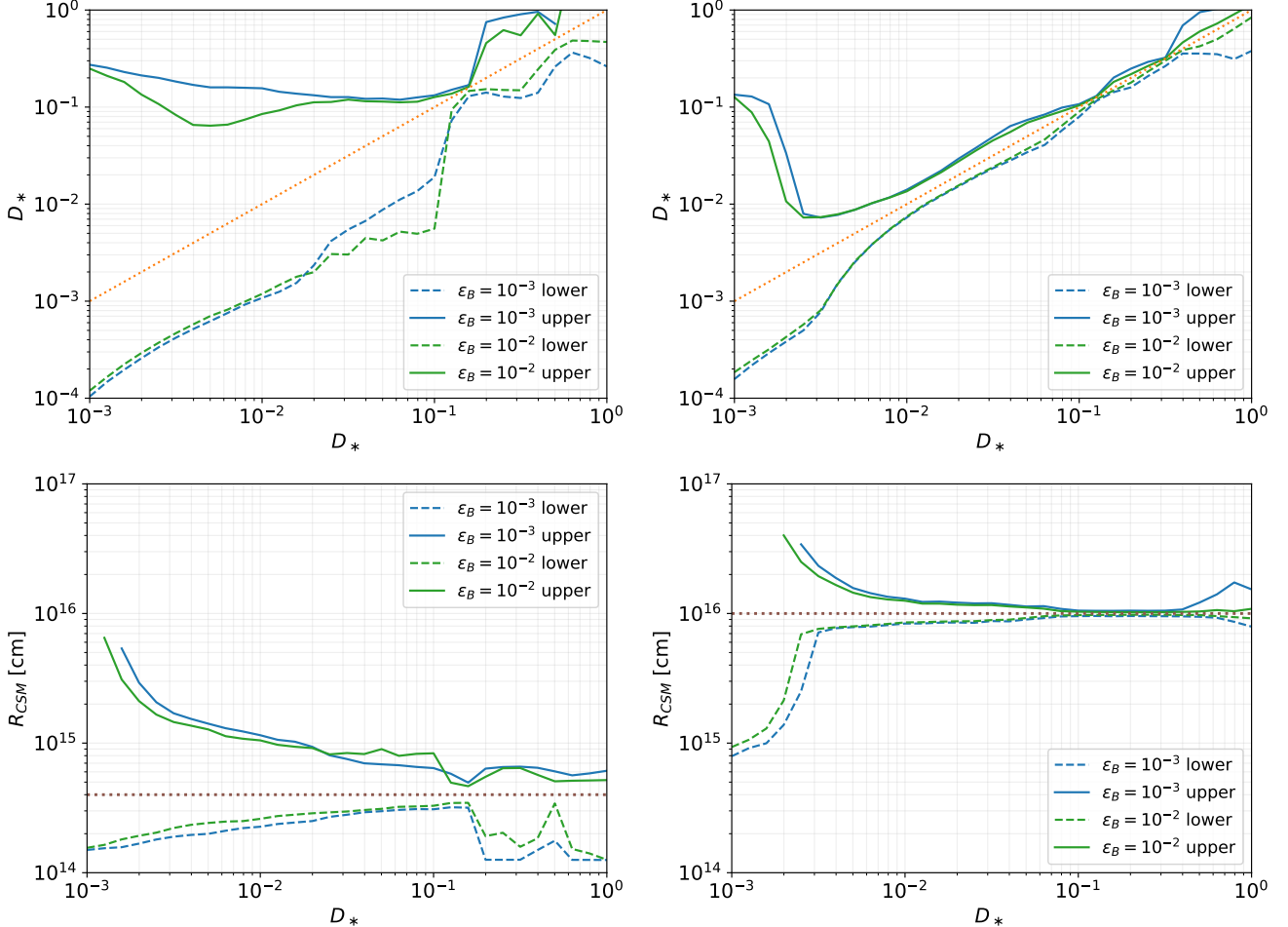


FIG. 9. One-dimensional constraints on the parameters D_* (upper) and R_{csm} (lower) for a Galactic Type II (left) and Type IIn (right) SN at distances of 10 kpc. The x -axis shows the D_* values of the benchmark model, with $R_{\text{csm}} = 4 \times 10^{14}$ cm (Type II) and 10^{16} cm (Type IIn), assuming $\epsilon_B = 10^{-3}$, 10^{-2} and $\epsilon_p = 0.1$. The y -axis denotes the projected 3σ lower and upper limits on D_* and R_{csm} using the HE neutrino signals.

10. We note that high event statistics significantly reduce the impact of parameter degeneracies, allowing R_{csm} , D_* , and ϵ_p to be constrained with similar precision.

As shown in the right panels of Figs. 9 and 10, the constraining power is further improved for SNe surrounded by extended CSM (Type IIn) at the same distance. For benchmark values of D_* from $\sim 3 \times 10^{-3}$ to ~ 0.5 , D_* , R_{csm} , and ϵ_p can be measured with a precision of ~ 20 –30%. Furthermore, for D_* between ~ 0.03 and ~ 0.7 , ϵ_B can also be constrained to a comparable level. These results are largely insensitive to the assumed benchmark values of ϵ_B (10^{-3} and 10^{-2}).

Overall, despite the large uncertainties and broad ranges of the relevant parameters, HE neutrino observations of a nearby SN with sufficient statistics and distinctive spectral and temporal features can constrain the CSM profile (D_* and R_{csm}) and the proton acceleration efficiency ϵ_p , while providing comparatively weaker but still meaningful constraints on ϵ_B . The modest parameter degeneracies identified in this analysis do not sig-

nificantly compromise these conclusions, especially when the event statistics are sufficiently large.

V. DISCUSSION AND CONCLUSION

In this work, we study HE neutrino production from interactions between the SN ejecta and the surrounding CSM, following the formalism of Refs. [40, 74]. We focus on regular Type II and Type IIn SNe, adopting observationally inferred distributions of the CSM density normalization D_* from large SN samples, as well as characteristic CSM extents R_{csm} . Within this framework, we explore the impact of key physical parameters—including D_* , R_{csm} , the proton acceleration efficiency ϵ_p , and the magnetic energy fraction ϵ_B —on the resulting neutrino flux. We also compare calculations with and without explicitly solving the time-dependent transport of accelerated protons, finding that proton transport introduces modest but non-negligible modifications to the predicted

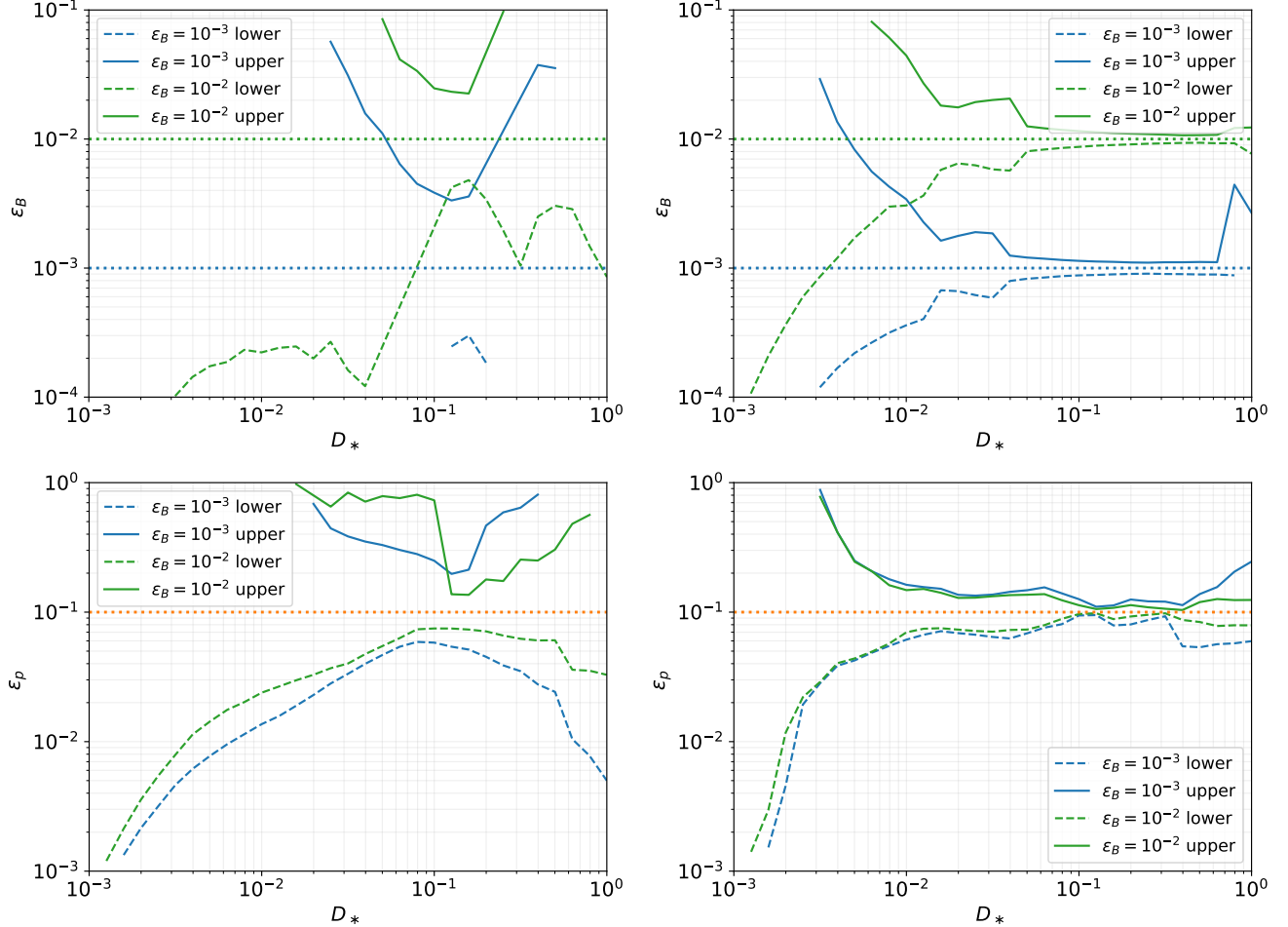


FIG. 10. Same as Fig. 9, but showing the constraints on ϵ_B (upper) and ϵ_p (lower) for Type II (left) and Type IIn (right) SNe.

HE neutrino signal.

We evaluate the detectability of these neutrinos using a binned likelihood approach in both time and energy, focusing on upgoing track events at IceCube. The detection prospects depend sensitively on the CSM profile and shock microphysics. For demonstration, we fix $\epsilon_p = 0.1$, adopt $R_{\text{csm}} = 4 \times 10^{14}$ cm and 10^{16} cm for Type II and Type IIn SNe, respectively, and consider two representative values of $\epsilon_B = 10^{-4}$ and 0.1 . We find an optimal density range $D_* \sim 0.03\text{--}0.3$ ($0.1\text{--}0.5$) for typical Type II (IIn) SNe, for which the detection horizon extends to $\sim 0.05\text{--}0.2$ Mpc ($0.15\text{--}0.6$ Mpc), depending on ϵ_B ($10^{-4}\text{--}0.1$). For Galactic SNe at distances of ~ 10 kpc, a broad range of CSM densities ($D_* \sim 10^{-3}\text{--}10$) can yield detectable signals at $\geq 3\sigma$. These results indicate that nearby regular Type II SNe with moderately dense, confined CSM are promising targets for HE neutrino observations, while Type IIn SNe represent the most luminous but rarer sources.

By integrating the neutrino emission over the cosmic CCSN rate, we also evaluate the diffuse neutrino flux contributed by the entire populations of Type II and Type

IIn SNe. We find that ordinary Type II SNe make a non-negligible contribution to the diffuse flux, owing to their substantially higher event rate and the existence of a tail of systems exhibiting enhanced, short-lived mass loss. Nevertheless, even under optimistic assumptions, the predicted diffuse flux remains well below the diffuse astrophysical neutrino intensity measured by IceCube. This indicates that targeted searches for neutrinos from nearby SNe are considerably more promising [41].

A key result of this work is that neutrino observations from a future Galactic Type II or Type IIn SN, with detailed spectral and temporal information, can place meaningful constraints on the CSM density profile and shock-acceleration parameters, despite their broad physically allowed ranges. Using profile-likelihood analyses for a Type II SN with $D_* = 0.01$ (and Type IIn SN with $D_* \sim 0.01\text{--}1$) at 10 kpc, we find that R_{csm} can be constrained to within a factor of ~ 2 (20%). By comparison, D_* and ϵ_p can be measured within a factor of ~ 10 (20%), while ϵ_B is weakly constrained for Type II SNe and to $\sim 20\%$ for Type IIn SNe. The constraining power increases with D_* , as shown in Figs. 9 and 10. Param-

eter degeneracies can reduce precision, but this effect is largely mitigated at higher event statistics corresponding to larger D_* or extended CSM, preserving the sensitivity of the neutrino signal. Although not explored in detail in this work, next-generation neutrino observatories such as IceCube-Gen2, KM3NeT, and TRIDENT will further extend the detection horizon and enhance parameter constraints.

We fix M_{ej} and \mathcal{E}_{ej} in our study, but variations in these quantities can be effectively absorbed into D_* [Eq. (4)]. We also adopt a canonical wind-like CSM profile with density slope $w = 2$ and a fixed proton acceleration index $p = 2$. While these assumptions may not apply to all progenitors, high-statistics neutrino observations with detailed temporal and spectral information are expected to remain sensitive to a broader parameter space. Over-

all, within the framework of a simple ejecta-CSM interaction model, we demonstrate that HE neutrino observations of a Galactic SN, with sufficient statistics and detailed energy-time information, can provide a meaningful and complementary probe of the CSM density profile and shock acceleration, beyond what is accessible with traditional electromagnetic observations.

ACKNOWLEDGMENTS

This work was supported in part by the National SKA Program of China (No. 2025SKA0110104), Guangdong Basic and Applied Basic Research Foundation (No. 2025A1515011082), and the “CUG Scholar” Scientific Research Funds at China University of Geosciences (Wuhan) [No. 2021108].

[1] H.-T. Janka, K. Langanke, A. Marek, G. Martinez-Pinedo, and B. Mueller, *Phys. Rept.* **442**, 38 (2007).

[2] H.-T. Janka, *Ann. Rev. Nucl. Part. Sci.* **62**, 407 (2012).

[3] A. Burrows, *Rev. Mod. Phys.* **85**, 245 (2013).

[4] H.-T. Janka, Neutrino emission from supernovae, in *Handbook of Supernovae*, edited by A. W. Alsabti and P. Murdin (Springer International Publishing, Cham, 2017) pp. 1575–1604.

[5] T. Fischer, G. Guo, K. Langanke, G. Martinez-Pinedo, Y.-Z. Qian, and M.-R. Wu, *Prog. Part. Nucl. Phys.* **137**, 104107 (2024).

[6] H. Suzuki, *PTEP* **2024**, 05B101 (2024).

[7] G. G. Raffelt, H.-T. Janka, and D. F. G. Fiorillo (2025).

[8] I. Tamborra and K. Murase, *Space Sci. Rev.* **214**, 31 (2018).

[9] I. Tamborra, *Nature Rev. Phys.* **7**, 285 (2025).

[10] P. Mészáros and E. Waxman, *Physical Review Letters* **87**, 171102 (2001).

[11] S. Razzaque, P. Mészáros, and E. Waxman, *Physical Review D* **68**, 083001 (2003).

[12] S. Razzaque, P. Mészáros, and E. Waxman, *Physical Review Letters* **93**, 181101 (2004).

[13] S. Ando and J. F. Beacom, *Phys. Rev. Lett.* **95**, 061103 (2005), arXiv:astro-ph/0502521.

[14] S. RAZZAQUE, P. MÉSZÁROS, and E. WAXMAN, *Modern Physics Letters A* **20**, 2351–2367 (2005).

[15] S. Horiuchi and S. Ando, *Phys. Rev. D* **77**, 063007 (2008), arXiv:0711.2580 [astro-ph].

[16] I. Bartos, B. Dasgupta, and S. Marka, *Phys. Rev. D* **86**, 083007 (2012).

[17] K. Murase and K. Ioka, *Physical Review Letters* **111**, 121102 (2013).

[18] N. Fraija, *Mon. Not. Roy. Astron. Soc.* **437**, 2187 (2014).

[19] D. Xiao and Z. G. Dai, *Astrophysical Journal* **790**, 59 (2014).

[20] A. Bhattacharya, R. Enberg, M. H. Reno, and I. Sarcevic, *JCAP* **1506**, 034.

[21] K. Varela, S. Sahu, A. F. O. Oliveros, and J. C. Sanabria, *European Physical Journal C* **75**, 289 (2015), 1411.7992.

[22] I. Tamborra and S. Ando, *Phys. Rev. D* **93**, 053010 (2016).

[23] N. Senno, K. Murase, and P. Meszaros, *Phys. Rev. D* **93**, 083003 (2016).

[24] N. Senno, K. Murase, and P. Mészáros, *JCAP* **01**, 025.

[25] P. B. Denton and I. Tamborra, *Astrophys. J.* **855**, 37 (2018).

[26] P. B. Denton and I. Tamborra, *JCAP* **04**, 058.

[27] H.-N. He, A. Kusenko, S. Nagataki, Y.-Z. Fan, and D.-M. Wei, *Astrophys. J.* **856**, 119 (2018).

[28] G. Guo, Y.-Z. Qian, and M.-R. Wu, *Phys. Rev. D* **108**, L021303 (2023), arXiv:2212.08266 [astro-ph.HE].

[29] P.-W. Chang, B. Zhou, K. Murase, and M. Kamionkowski, *Phys. Rev. D* **109**, 103041 (2024).

[30] E. Guarini, I. Tamborra, and O. Gottlieb, *Phys. Rev. D* **107**, 023001 (2023).

[31] B. Zhang, Z. G. Dai, and P. Meszaros, *Astrophys. J.* **595**, 346 (2003).

[32] S. Nagataki, *Astrophys. J.* **600**, 883 (2004).

[33] K. Murase, P. Mészáros, and B. Zhang, *Physical Review D* **79**, 103001 (2009).

[34] K. Fang, *JCAP* **06**, 004, arXiv:1411.2174 [astro-ph.HE].

[35] K. Murase, T. A. Thompson, B. C. Lacki, and J. F. Beacom, *Phys. Rev. D* **84**, 043003 (2011).

[36] A. Gal-Yam *et al.*, *Nature* **509**, 471 (2014), arXiv:1406.7640 [astro-ph.HE].

[37] O. Yaron *et al.*, *Nature Phys.* **13**, 510 (2017), arXiv:1701.02596 [astro-ph.HE].

[38] V. N. Zirakashvili and V. S. Ptuskin, *Astropart. Phys.* **78**, 28 (2016), arXiv:1510.08387 [astro-ph.HE].

[39] M. Petropoulou, S. Coenders, G. Vasilopoulos, A. Kamble, and L. Sironi, *Mon. Not. Roy. Astron. Soc.* **470**, 1881 (2017), arXiv:1705.06752 [astro-ph.HE].

[40] K. Murase, *Phys. Rev. D* **97**, 081301 (2018), arXiv:1705.04750 [astro-ph.HE].

[41] A. Kheirandish and K. Murase, *Astrophys. J. Lett.* **956**, L8 (2023), arXiv:2204.08518 [astro-ph.HE].

[42] D. Guetta, A. Langella, S. Gagliardini, and M. Della Valle, *Astrophys. J. Lett.* **955**, L9 (2023), arXiv:2306.14717 [astro-ph.HE].

[43] S. S. Kimura and T. J. Moriya, *Astrophys. J.* **984**, 103 (2025), arXiv:2409.18935 [astro-ph.HE].

[44] S. P. Cosentino, M. L. Pumo, and S. Cherubini, (2025), arXiv:2503.03699 [astro-ph.HE].

[45] J. Vandembroucke *et al.* (IceCube), PoS **ICRC2025**, 1109 (2025), arXiv:2507.07097 [astro-ph.HE].

[46] R. Stein *et al.*, (2025), arXiv:2508.08355 [astro-ph.HE].

[47] M.-X. Lu, Y.-F. Liang, X.-G. Wang, and H.-Q. Zhang, (2025), arXiv:2508.19080 [astro-ph.HE].

[48] S. Garrappa *et al.*, (2025), arXiv:2512.07936 [astro-ph.HE].

[49] S. M. Adams, C. S. Kochanek, J. F. Beacom, M. R. Vagins, and K. Z. Stanek, *Astrophys. J.* **778**, 164 (2013), arXiv:1306.0559 [astro-ph.HE].

[50] K. Rozwadowska, F. Vissani, and E. Cappellaro, *New Astron.* **83**, 101498 (2021), arXiv:2009.03438 [astro-ph.HE].

[51] C. D. Matzner and C. F. McKee, *Astrophys. J.* **510**, 379 (1999), arXiv:astro-ph/9807046.

[52] T. J. Moriya, K. Maeda, F. Taddia, J. Sollerman, S. I. Blinnikov, and E. I. Sorokina, *Mon. Not. Roy. Astron. Soc.* **435**, 1520 (2013), arXiv:1307.2644 [astro-ph.HE].

[53] N. Smith, *Ann. Rev. Astron. Astrophys.* **52**, 487 (2014), arXiv:1402.1237 [astro-ph.SR].

[54] M. Kiewe, A. Gal-Yam, I. Arcavi, D. C. Leonard, J. Emilio Enriquez, S. B. Cenko, D. B. Fox, D.-S. Moon, D. J. Sand, A. M. Soderberg, and T. CCCP, *The Astrophysical Journal* **744**, 10 (2012).

[55] F. Taddia *et al.*, *Astron. Astrophys.* **555**, A10 (2013), arXiv:1304.3038 [astro-ph.CO].

[56] T. J. Moriya, K. Maeda, F. Taddia, J. Sollerman, S. I. Blinnikov, and E. I. Sorokina, *Mon. Not. Roy. Astron. Soc.* **439**, 2917 (2014), arXiv:1401.4893 [astro-ph.SR].

[57] P. Sarmah, S. Chakraborty, I. Tamborra, and K. Auchettl, *JCAP* **08** (08), 011, arXiv:2204.03663 [astro-ph.HE].

[58] C. L. Ransome and V. A. Villar, *Astrophys. J.* **987**, 13 (2025), arXiv:2409.10596 [astro-ph.HE].

[59] I. Salmaso *et al.*, *Astron. Astrophys.* **695**, A29 (2025), arXiv:2410.06111 [astro-ph.HE].

[60] D. Khazov *et al.*, *Astrophys. J.* **818**, 3 (2016), arXiv:1512.00846 [astro-ph.HE].

[61] V. S. Morozova, A. L. Piro, and S. Valenti, *The Astrophysical Journal* **838** (2016).

[62] V. Morozova, A. L. Piro, and S. Valenti, *Astrophys. J.* **858**, 15 (2018), arXiv:1709.04928 [astro-ph.HE].

[63] F. Förster *et al.*, *Nature Astron.* **2**, 808 (2018), [Erratum: *Nature Astron.* 3, 107 (2019)], arXiv:1809.06379 [astro-ph.HE].

[64] T. J. Moriya, F. Förster, S.-C. Yoon, G. Gräfener, and S. I. Blinnikov, *Mon. Not. Roy. Astron. Soc.* **476**, 2840 (2018), arXiv:1802.07752 [astro-ph.HE].

[65] W. V. Jacobson-Galán *et al.*, *Astrophys. J.* **970**, 189 (2024), arXiv:2403.02382 [astro-ph.HE].

[66] R. J. Bruch *et al.*, *Astrophys. J.* **912**, 46 (2021), arXiv:2008.09986 [astro-ph.HE].

[67] R. J. Bruch *et al.*, *Astrophys. J.* **952**, 119 (2023), arXiv:2212.03313 [astro-ph.HE].

[68] J. Silva-Farfán, F. Förster, T. J. Moriya, L. Hernández-García, A. M. M. Arancibia, P. Sánchez-Sáez, J. P. Anderson, J. L. Tonry, and A. Clocchiatti, *Astrophys. J.* **969**, 57 (2024), arXiv:2404.12620 [astro-ph.HE].

[69] K.-R. Hinds *et al.* 10.1093/mnras/staf888 (2025), arXiv:2503.19969 [astro-ph.HE].

[70] S. Tinyanont *et al.*, *Mon. Not. Roy. Astron. Soc.* **512**, 2777 (2022), arXiv:2110.10742 [astro-ph.SR].

[71] M. Shrestha *et al.*, *Astrophys. J. Lett.* **972**, L15 (2024), arXiv:2405.18490 [astro-ph.HE].

[72] M. Hu, L. Wang, and X. Wang, *Astrophys. J.* **984**, 44 (2025), arXiv:2411.06351 [astro-ph.HE].

[73] M. Hu, Y. Ao, Y. Yang, L. Hu, F. Li, L. Wang, and X. Wang, *Astrophys. J. Lett.* **978**, L27 (2025), arXiv:2412.11389 [astro-ph.SR].

[74] T. Pitik, I. Tamborra, M. Lincetto, and A. Franckowiak, *Mon. Not. Roy. Astron. Soc.* **524**, 3366 (2023), arXiv:2306.01833 [astro-ph.HE].

[75] R. A. Chevalier, *Astrophys. J.* **258**, 790 (1982).

[76] R. A. Chevalier, *Astrophys. J.* **259**, 302 (1982).

[77] R. A. Chevalier and C. Fransson, *Astrophys. J.* **420**, 268 (1994).

[78] A. Suzuki, T. J. Moriya, and T. Takiwaki, *Astrophys. J.* **899**, 56 (2020).

[79] J. P. Ostriker and C. F. McKee, *Reviews of Modern Physics* **60**, 1 (1988).

[80] C. Bierlich *et al.*, *SciPost Phys. Codeb.* **2022**, 8 (2022), arXiv:2203.11601 [hep-ph].

[81] G. Guo, Y.-Z. Qian, and M.-R. Wu, *Phys. Rev. D* **112**, 063022 (2025), arXiv:2506.17581 [astro-ph.HE].

[82] Z.-Z. Xiao, G. Guo, and T. Tuniyazi, *Phys. Rev. D* **112**, 063047 (2025), arXiv:2507.16551 [astro-ph.HE].

[83] M. G. Aartsen *et al.* (IceCube), *JINST* **12** (03), P03012, [Erratum: *JINST* 19, E05001 (2024)], arXiv:1612.05093 [astro-ph.IM].

[84] M. Ageron and Others, *Nuclear Instruments and Methods in Physics Research A* **656**, 11 (2011).

[85] S. Adrian-Martinez *et al.* (KM3Net), *J. Phys. G* **43**, 084001 (2016), arXiv:1601.07459 [astro-ph.IM].

[86] M. G. Aartsen *et al.* (IceCube-Gen2), *J. Phys. G* **48**, 060501 (2021), arXiv:2008.04323 [astro-ph.HE].

[87] M. Agostini *et al.* (P-ONE), *Nature Astron.* **4**, 913 (2020), arXiv:2005.09493 [astro-ph.HE].

[88] Z. P. Ye *et al.* (TRIDENT), *Nature Astron.* **7**, 1497 (2023), arXiv:2207.04519 [astro-ph.HE].

[89] M. G. Aartsen *et al.* (IceCube), *Phys. Rev. Lett.* **115**, 081102 (2015), arXiv:1507.04005 [astro-ph.HE].

[90] M. G. Aartsen *et al.* (IceCube, Fermi-LAT, MAGIC, AGILE, ASAS-SN, HAWC, H.E.S.S., INTEGRAL, Kanata, Kiso, Kapteyn, Liverpool Telescope, Subaru, Swift NuSTAR, VERITAS, VLA/17B-403), *Science* **361**, eaat1378 (2018), arXiv:1807.08816 [astro-ph.HE].

[91] M. G. Aartsen *et al.*, *Science* **361**, 147–151 (2018).

[92] R. Abbasi *et al.*, *Science* **378**, 538–543 (2022).

[93] S. Aiello *et al.* (KM3NeT), *Nature* **638**, 376 (2025), [Erratum: *Nature* 640, E3 (2025)].

[94] R. Abbasi *et al.*, (2025), arXiv:2510.13403 [astro-ph.HE].

[95] M. G. Aartsen *et al.* (IceCube), *Astrophys. J.* **886**, 12 (2019), arXiv:1907.06714 [astro-ph.HE].

[96] R. Abbasi *et al.* (IceCube), *Science* **380**, adc9818 (2023), arXiv:2307.04427 [astro-ph.HE].

[97] R. Abbasi *et al.* (IceCube), *Phys. Rev. D* **110**, 022001 (2024), arXiv:2402.18026 [astro-ph.HE].

[98] Evidence for Astrophysical Muon Neutrinos from the Northern Sky with IceCube.

[99] <https://github.com/afedynitch/MCEq>.

[100] R. Abbasi *et al.*, *Astrophys. J.* **928**, 50 (2022), arXiv:2111.10299 [astro-ph.HE].

[101] G. Cowan, K. Cranmer, E. Gross, and O. Vitells, *Eur. Phys. J. C* **71**, 1554 (2011), [Erratum: *Eur.Phys.J.C* 73,

2501 (2013)], arXiv:1007.1727 [physics.data-an].

[102] X. Ma *et al.*, Astron. Astrophys. **698**, A306 (2025).

[103] X. Ma *et al.*, Astron. Astrophys. **698**, A305 (2025).

[104] Y. Ashida, (2024), arXiv:2401.12403 [astro-ph.HE].

[105] R. Abbasi *et al.* (IceCube), Astrophys. J. Lett. **949**, L12 (2023), arXiv:2303.03316 [astro-ph.HE].